BRAIN ANATOMY

A mesothelium divides the subarachnoid space into functional compartments

Kjeld Møllgård[1]*†, Felix R. M. Beinlich[2]†, Peter Kusk[2]†, Leo M. Miyakoshi[2]†, Christine Delle[2], Virginia Plá[2], Natalie L. Hauglund[2], Tina Esmail[2], Martin K. Rasmussen[2], Ryszard S. Gomolka[2], Yuki Mori[2], Maiken Nedergaard[3]*

The central nervous system is lined by meninges, classically known as dura, arachnoid, and pia mater. We show the existence of a fourth meningeal layer that compartmentalizes the subarachnoid space in the mouse and human brain, designated the subarachnoid lymphatic-like membrane (SLYM). SLYM is morpho- and immunophenotypically similar to the mesothelial membrane lining of peripheral organs and body cavities, and it encases blood vessels and harbors immune cells. Functionally, the close apposition of SLYM with the endothelial lining of the meningeal venous sinus permits direct exchange of small solutes between cerebrospinal fluid and venous blood, thus representing the mouse equivalent of the arachnoid granulations. The functional characterization of SLYM provides fundamental insights into brain immune barriers and fluid transport.

Emerging evidence supports the concept that cerebrospinal fluid (CSF) acts as a quasi-lymphatic system in the central nervous system (*1*). Cardiovascular pulsatility drives CSF inflow along periarterial spaces into deep brain regions (*2*, *3*), where CSF exchange with interstitial fluid, facilitated by glial aquaporin 4 (AQP4) water channels (*4*), takes place. Fluid and solutes from the neuropil are cleared along multiple routes, including perivenous spaces and cranial nerves, for ultimate export to the venous circulation via meningeal and cervical lymphatic vessels (*5*, *6*). CSF reabsorption may also occur at the sinuses via the arachnoid granulations—although this has not been described in rodents (*7*–*10*). Despite the efforts dedicated to studying CSF flow along the glymphatic-lymphatic path, it remains to be determined how CSF is transported within the large cavity of the subarachnoid space (*11*, *12*). In this study, we explored how CSF and immune cell trafficking are organized within the subarachnoid space surrounding the brains of mice and humans.

The meningeal membranes were first analyzed by in vivo two-photon microscopy in the somatosensory cortex of Prox1-EGFP$^+$ reporter mice (Prox1, prospero homeobox protein 1; EGFP, enhanced green fluorescent protein). Prox1 is a transcription factor that determines lymphatic fate (*13*, *14*). Second harmonic generation was used to visualize unlabeled collagen fibers, while the vascular volume was labeled by a Cascade Blue conjugated dextran, and astrocytes were labeled by sulforhodamine 101 (SR101, intraperitoneally) (*15*, *16*). Below the parallel-oriented collagen bundles in dura, we noted a continuous monolayer of flattened Prox1-EGFP$^+$ cells intermixed with loosely organized collagen fibers. This subarachnoid lymphatic-like membrane (SLYM) divides the subarachnoid space into an outer superficial compartment and an inner deep compartment lining the brain (Fig. 1A). Quantitative in vivo analysis of the somatosensory cortex revealed that the thickness of SLYM itself was 14.2 ± 0.5 μm, hence thinner than dura (21.8 ± 1.3 μm, n = 6 mice). The dura vasculature is surrounded by collagen fibers, whereas SLYM covers the subarachnoid vessels. The organization and calibers of the two sets of vasculature also exhibit distinct differences (Fig. 1, B and C).

A key question is whether SLYM constitutes an impermeable membrane that functionally compartmentalizes the subarachnoid space. To test this, Prox1-EGFP$^+$ mice were first injected with 1-μm microspheres conjugated to a red fluorophore into the subdural outer superficial compartment of the subarachnoid space along with an injection of 1-μm microspheres conjugated to a blue fluorophore distributed within the inner deep subarachnoid space compartment by cisterna magna injection (Fig. 2A). In vivo two-photon microscopy showed that the red microspheres were confined to the outer superficial compartment, whereas the blue microspheres remained trapped in the inner deep subarachnoid space compartment. Quantitative analysis showed that the 1-μm microspheres did not cross SLYM from either side. Yet, many solutes in CSF, such as cytokines and growth factors, are considerably smaller than 1 μm in diameter (*17*). Therefore, we sought to determine whether a small tracer could pass through SLYM. In these experiments, tetramethylrhodamine (TMR)–dextran (3 kDa) was administered into the deep inner subarachnoid space via the cisterna magna in Prox1-EGFP$^+$ mice. In six mice, the small tracer did not cross the EGFP-expressing

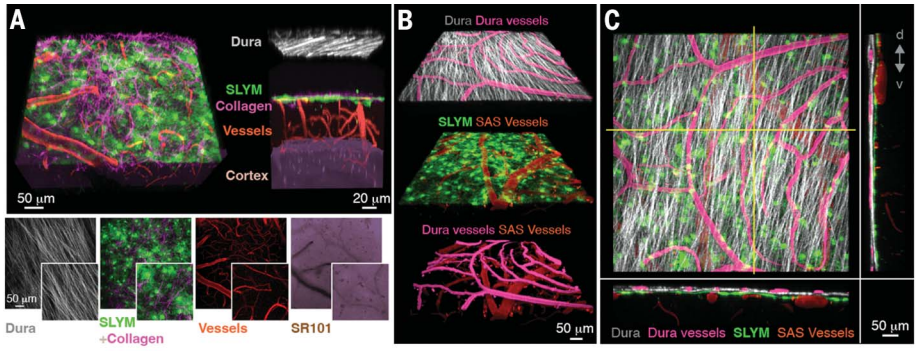

Fig. 1. In vivo imaging depicts a fourth meningeal layer. (**A**) In vivo two-photon imaging of Prox1-EGFP$^+$ reporter mice viewed through a closed cranial window placed over the somatosensory cortex. Maximum projection and three-dimensional (3D) views depict the spatial distribution of dura mater collagen fibers (gray) detected by second harmonic generation. Prox1-EGFP$^+$ cells (green) intermixed with the irregular sparse collagen fibers (purple) localized below dura. This subarachnoid lymphatic-like membrane is abbreviated SLYM. Blood vessels outlined by Cascade Blue conjugated dextran (red, 10 kDa, iv) are located at the cortical surface. (Inset) A lateral view of the 3D reconstruction with all the layers displayed individually along the z axis to facilitate spatial comprehension. (**B**) Two-photon imaging over the sensorimotor cortex in a Prox1-EGFP reporter mouse. The vasculature was outlined by intravenous injection of TMR-dextran (2000 kDa), and z-stacks were collected. Representative 3D reconstruction of the z-stacks. The vasculature in dura (magenta) is embedded in collagen fibers (white). In contrast, the vasculature in the subarachnoid space (red) is overlaid by SLYM (green). (**C**) Orthogonal sections through the z-stack show that the vasculature in dura is surrounded by collagen fibers. SLYM is located beneath dura, in close apposition with the large-caliber subarachnoid vessels.

[1]Department of Cellular and Molecular Medicine, Faculty of Health and Medical Sciences, University of Copenhagen, 2200 Copenhagen, Denmark. [2]Division of Glial Disease and Therapeutics, Center for Translational Neuromedicine, Faculty of Health and Medical Sciences, University of Copenhagen, 2200 Copenhagen, Denmark. [3]Division of Glial Disease and Therapeutics, Center for Translational Neuromedicine, University of Rochester Medical Center, Rochester, NY 14642, USA.
***Corresponding author. Email: nedergaard@urmc.rochester.edu (M.N.); kjm@sund.ku.dk (K.M.)**
†These authors contributed equally to this work.

SLYM (Fig. 2B and fig. S1). Yet, in mice with dural damage and leakage of CSF, the tracer was observed on both sides of the EGFP$^+$ membrane (fig. S1). Thus, SLYM divides the subarachnoid space into an upper superficial and a lower deep compartment for solutes ≥3 kDa. SLYM is therefore a barrier that limits the exchange of most peptides and proteins, such as amyloid-β and tau, between the upper and lower subarachnoid space compartments.

Live brain imaging avoids fixation artifacts (*18*) but cannot immunophenotypically characterize the meningeal membranes. To preserve the integrity of the meningeal membranes, sections were next obtained from whole heads of Prox1-EGFP$^+$ mice. Immunohistochemistry revealed that Prox1-EGFP$^+$ cells lined the ventral parts of the entire brain surface (Fig. 3A). Immunolabeling showed that the Prox1-EGFP$^+$ SLYM cells were positive for another lymphatic marker, podoplanin (PDPN) (*19*), but not for the lymphatic vessel endothelial receptor 1 (LYVE1) (*20*) (Fig. 3, A, lower right panels, and D). SLYM also labeled for the cellular retinoic acid–binding protein 2 (CRABP2) (Fig. 3, A and D), which is restrictively expressed in dural and arachnoid cells during early development (*21*). In contrast to SLYM, lymphatic vessels in dura were positive for all the classical lymphatic antigens, Prox1-EGFP$^+$, PDPN$^+$, LYVE1$^+$, and VEGFR3$^+$, but was CRABP2$^-$ (fig. S2). Notably, analysis of adult human cerebral cortex depicted that above the pia mater, a CRABP2$^+$/PDPN$^+$ membrane was present in the entire subarachnoid space (Fig. 3, B and C). Thus, SLYM also surrounds the human brain. We

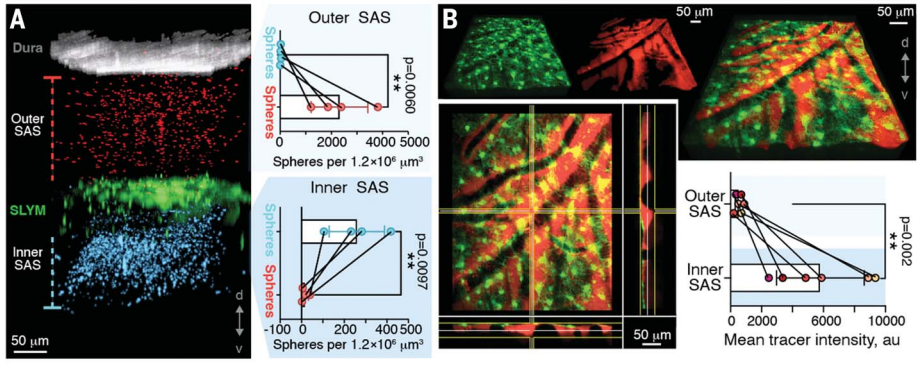

Fig. 2. SLYM represents a barrier that subdivides the subarachnoid space into two compartments. (**A**) Representative image of a 3D view of maximum projection collected after dual injections of red microspheres (red, 1 µm) into the outer superficial subarachnoid space (subdural) and blue microspheres delivered into the inner deep subarachnoid space by cisterna magna injection (blue, 1 µm) in a Prox1-EGFP$^+$ mouse. Graphs show a comparison of red microspheres versus blue microspheres detected in both the outer and inner subarachnoid space (SAS). Two-tailed unpaired *t* test; outer SAS, $P < 0.01$; inner SAS, $P < 0.01$; $n = 4$ mice. (**B**) Representative in vivo *z*-stack of a Prox1-EGFP mouse injected with a 3-kDa TMR-conjugated dextran CSF tracer delivered via the cisterna magna. Upper panels depict SLYM (green) and the perivascular distribution of the dextran (red) as well as the two channels merged. Lower panel displays the merge of the two channels and orthogonal optical sections showing that tracer is confined to below the membrane. Graph shows the mean tracer intensity detected below and above the membrane. Two-tailed unpaired *t* test with Welch's correction, $P < 0.01$, $n = 6$ mice. Significance shown as $^{**}P < 0.01$. au, arbitrary units; CM, cisterna magna; d, dorsal; v, ventral.

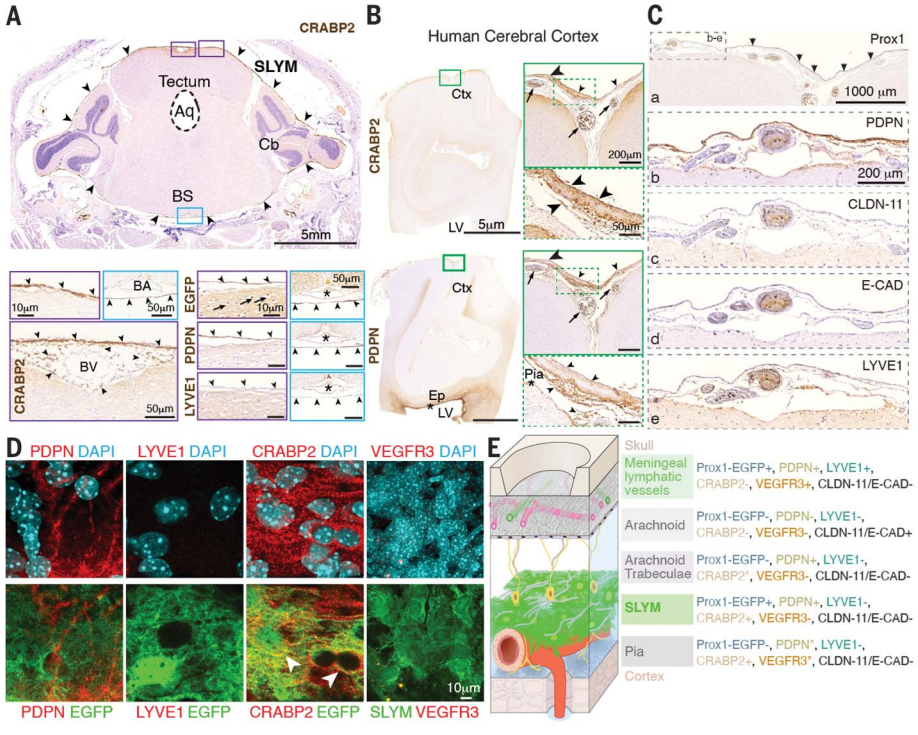

Fig. 3. Immunophenotypic characterization of SLYM in the mouse and human brain. (**A**) Sections of Prox1-EGFP$^+$ mouse brain after decalcification of the whole head counterstained with Mayer's hematoxylin (M-HE, purple) show that SLYM (arrowheads) is positively immunolabeled for CRABP2 (brown) and Prox1-EGFP$^+$/PDPN$^+$/LYVE1$^-$/VEGFR3$^-$ and encases the entire brain, covering its dorsal and ventral portions (purple and blue insets, respectively). (**B**) Adult human brain sections immunolabeled for CRABP2 and PDPN reveal the presence of SLYM (arrowheads) that enwraps the subarachnoid space blood vessels (arrow). Ependymal and pia mater cells are also PDPN$^+$ (asterisks). (**C**) Serial sections of the same adult human material immunolabeled for Prox1, PDPN, CLDN11, E-CAD, and LYVE1. SLYM is indicated by arrowheads. (**D**) Confocal images of SLYM immunolabeling showing positive labeling for PDPN and CRABP2 (both in red). No signal was detected for LYVE1 or VEGFR3. (**E**) Schematic representations of the immunophenotypical characterization of the meningeal layers, meningeal lymphatic vessels, and arachnoid trabeculations. For arachnoid trabeculae, CRABP2* signifies that the trabeculae are CRABP2$^-$ in the outer SAS but CRABP2$^+$ in the inner SAS. For pia, PDPN* indicates that pia is PDPN$^+$ in many regions of pia, but not all. VEGFR3* signifies that pia was VEGFR3$^+$ only in a few regions. Aq, aqueduct; BA, basilar artery; BS, brain stem; BV, blood vessel; Cb, cerebellum; Ctx, cerebral cortex; Ep, ependyma; LV, lateral ventricle.

infer that the SLYM monolayer of Prox1-EGFP$^+$ cells organizes into a membrane rather than vessel structures and exhibits a distinctive set of lymphatic markers (Fig. 3E). To distinguish SLYM from the structures forming the arachnoid mater, we used immunolabeling against claudin-11 (CLDN-11), a main constituent of the tight junctions that create the arachnoid barrier cell layer (ABCL) (*22*). CLDN-11 was densely expressed in ABCL as well as in the stromal cells of the choroid plexus, but SLYM was CLDN-11$^-$ (fig. S3, A and B). Additionally, ABCL was distinctively positive for E-cadherin (E-Cad) (Fig. 3C), as previously reported (*23*, *24*). We also compared SLYM to the arachnoid trabeculae (*25*), collagen-enriched structures that span the subarachnoid space, finding that cells surrounding the arachnoid trabeculae are Prox1-EGFP$^-$/LYVE1$^-$ (fig. S3C). Pial cells covering the cortical surface also exhibited an immune-labeling profile that differed from that of SLYM (figs. S3 and S4). We conclude that SLYM constitutes a fourth meningeal layer surrounding the mouse and human brain displaying lymphatic-like features (Prox1-EGFP$^+$, PDPN$^+$, LYVE1$^-$, CRABP2$^+$, VEGFR3$^-$, CLDN-11$^-$, and E-Cad$^-$) and that SLYM is phenotypically distinct from dura, the arachnoid, and pia mater (Fig. 3E). Interestingly, SLYM expressed PDPN, sharing a trait with the mesothelium lining the body cavities (*26*). Accordingly, we observed PDPN$^+$ cells lining the kidney, as well as PDPN$^+$ podocytes in the kidneys of adult C57BL/6J mice (fig. S5A). In a human fetus, a PDPN$^+$ membrane corresponding to pericardium, pleura, and peritoneum encases the developing heart, lungs, and intestinal tract, respectively. PDPN$^+$ lymphatic vessels were also observed in the lungs and intestinal tract (fig. S5, B and C). Thus, SLYM may represent the brain mesothelium and, as such, covers blood vessels in the subarachnoid space (Fig. 1) (*26*). The mesothelium is present where tissues slide against each other and is believed to act as a boundary lubricant to ease movement (*27*). Physiological pulsations induced by the cardiovascular system, respiration, and positional changes of the head are constantly shifting the brain within the cranial cavity. SLYM may, like other mesothelial membranes, reduce friction between the brain and skull during such movements.

Does SLYM have additional functions? The arachnoid villi and granulations are defined as protrusions of the arachnoid membrane into the lateral walls of the sinus veins and are believed to act as passive filters that drain

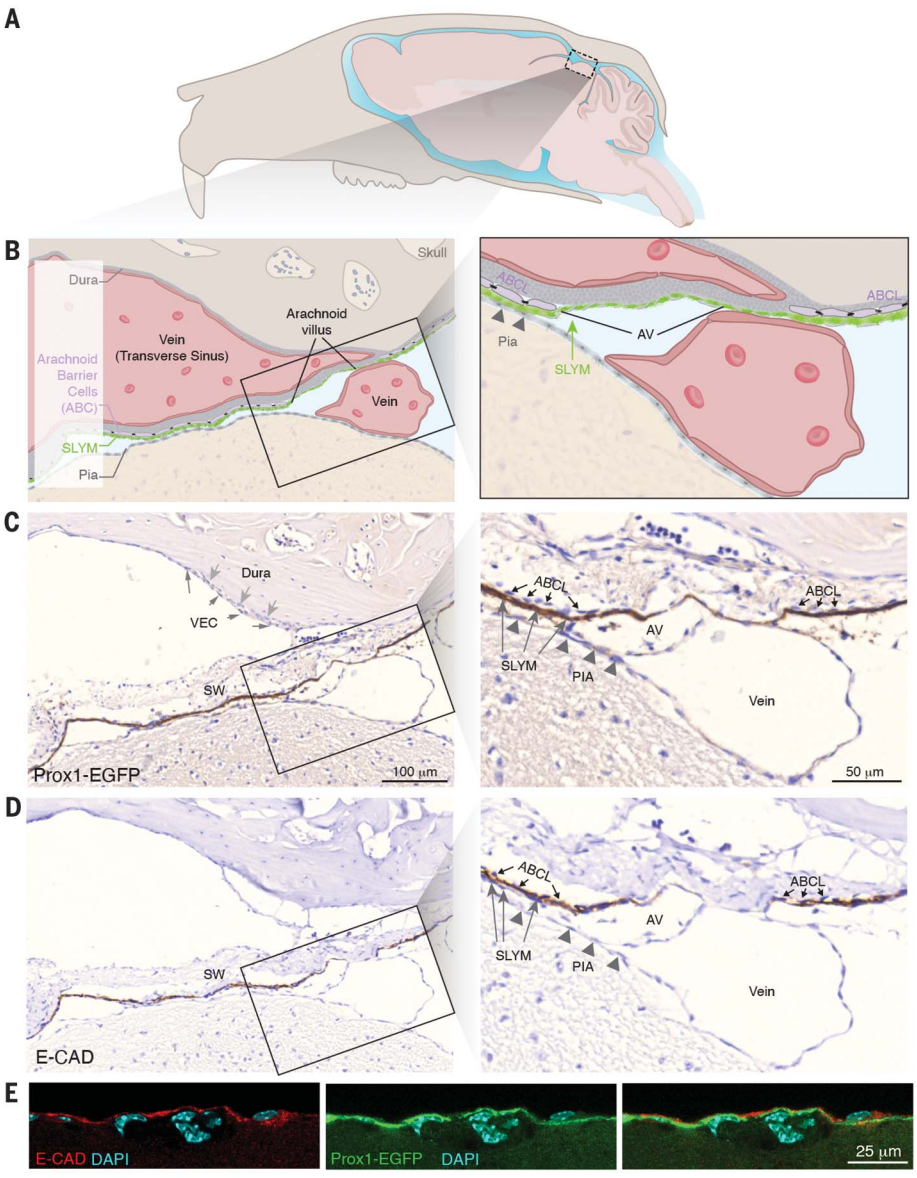

Fig. 4. SLYM forms subarachnoid villus–like structures at the venous sinus walls in mice. (**A** and **B**) Schematic diagrams illustrating the region of interest. (**C** and **D**) Parasagittal consecutive sections from a decalcified mouse whole head stained for (C) the SLYM marker Prox1-EGFP and (D) the arachnoid barrier cell marker E-Cad. Rectangular insets on the left in (B), (C), and (D) are shown in higher magnification on the right. A Prox1-positive arachnoid villus–like structure (AV) and a vein from the dorsal venous system are in direct contact with the transverse sinus wall (SW), which is lacking an intervening ABCL [inset in (C) and (D)]. The ABCL [arrows in inset in (C)] are not stained for Prox1, in contrast to the strongly stained SLYM layer, whereas the opposite pattern of reactivity is depicted in the adjacent section [inset in (D)], where ABCL is positive for E-Cad and SLYM is negative. Arrowheads point to pia. In (C), the narrow dura layer, indicated by small arrows, is facing the venous endothelial layer (VEC), indicated by slender darker arrows. (C) and (D) are the same magnification, as are their insets. (**E**) Confocal imaging of Prox1-EGFP and E-Cad shows that the signals do not colocalize.

CSF from the subarachnoid space into the venous sinus system (*7*–*10*). The arachnoid villi and granulations are present in the brains of humans, primates, and larger animals such as dogs, but not in the brains of rodents (*28*, *29*). We critically reexamined this issue to evaluate the distribution of SLYM in relation to the superior sagittal and transverse sinus. Sections obtained from decalcified heads of Prox1-EGFP$^+$ mice showed that Prox1-EGFP$^+$ SLYM cells often were in direct contact with the venous sinus endothelial cells (Fig. 4A). Thus, the arachnoid barrier cell layer (CLDN-11$^+$/E-Cad$^+$), which normally separates dura from the subarachnoid space, was lacking in discrete areas allowing SLYM to directly contact the venous sinus wall (Fig. 4B). Prox1-EGFP$^+$ SLYM cells were not positive for CLDN-11 or E-Cad, which distinguish the arachnoid barrier cell layer (fig. S6).

Are the close appositions of SLYM and the venous endothelial cells permeable, allowing the exchange of small molecules between blood and CSF? To test this, we used the principles of bioluminescence, wherein the convergence, in the same compartment, of an enzyme with its substrate is needed to trigger light emission. First, we delivered the luciferase enzyme from *Oplophorus gracilirostris* (NanoLuc) fused to the fluorescence tag mNeongreen (GeNL, 44 kDa) (*30*) into CSF via the cisterna magna of wild-type (C57bl/6) mice, and allowed it to circulate for 30 min to ensure thorough distribution by the glymphatic system. The distribution of GeNL was verified by mNeongreen fluorescence. Then, the blood-brain barrier (BBB)–impermeable substrate fluorofurimazine (FFz, 433 Da) (*31*) was administered intravenously (fig. S7, A to C) (*32*). After intravenous injection of FFz, a bright bioluminescence signal catalyzed by GeNL was detected specifically near the large venous sinus wall (fig. S7, A and B). The bioluminescence signal was particularly strong around the confluence of sinuses (fig. S7B). The distribution of the bioluminescence signal was quantified by plotting the mean signal intensity profiles perpendicular to the venous wall of the transverse sinus and superior sagittal sinus. The mean bioluminescence signal profiles intersected with the fluorescence signal profiles of the intravascular tracer (TMR-dextran, 70 kDa) or with shadow imaging of the inverted GeNL signal outlining the vascular wall (fig. S7C). Thus, the bioluminescence signal was restricted to the venous wall of the two major sinuses lacking a BBB (*33*, *34*), consistent with the notion that FFz is BBB-impermeable and requires the catalyzation enzyme NanoLuc to generate photons (fig. S7, A to C). In control experiments, FFz was delivered intravenously, while the GeNL injection into CSF was omitted. In these control experiments, no bioluminescence signal was detected from the exposed cortex, including from the sinus venous wall (fig. S7D). In another set of control experiments, GeNL was injected into the soft ear tissue, while FFz was delivered intravenously. Consistent with the notion that peripheral blood vessels are leaky (*11*), light emission was clearly observed in the region of the ear injected with NanoLuc but not in surrounding noninjected regions of the same ear. No signal was observed in the venous compartment, likely reflecting that blood flow rapidly diluted the bioluminescence signal (fig. S7E). Together, this analysis shows that a small molecule, FFz, can enter the central nervous system (CNS) from the blood and activate an enzyme, NanoLuc, present in CSF, resulting in the generation of photons along the wall of the venous sinus. On the basis of the juxtaposition of SLYM and the venous endothelium in histological examination (Fig. 4A), the selective generation of photons when luciferase was injected into CSF, and the fact that the substrate was present in the vascular compartment (fig. S7, A to C), we propose that the apposition of the venous endothelia and SLYM represents rodent arachnoid villus–like structures, comparable to those in human brain.

The mesothelium surrounding peripheral organs acts as an immune barrier (*26*). Does SLYM also impede the entry of exogenous particles into CSF? In vivo two-photon imaging of Prox1-EGFP$^+$ mice injected intravenously with rhodamine 6G (Rhod6G) to label leukocytes (*35*) showed that a large number of Rhod6G$^+$ myeloid cells are embedded in SLYM (Fig. 5A). The number of Rhod6G$^+$ leukocytes in dura and SLYM was directly comparable, suggesting a prominent role of SLYM in CNS immune responses, which supports the finding that leptomeninges are densely populated with immune cells (*36*) (Fig. 5A). How do systemic inflammation and aging affect the immune cell populations residing in SLYM? Ex vivo analysis of brain sections obtained from Prox1-EGFP$^+$ mice showed that,

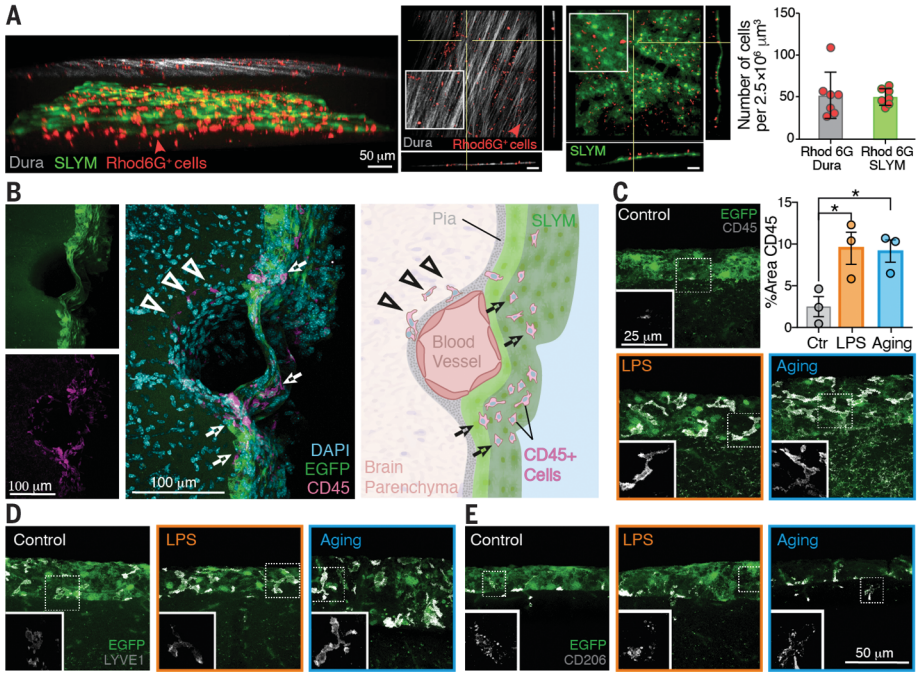

Fig. 5. SLYM hosts a large number of myeloid cells. (**A**) (Left) In vivo two-photon microscopy of Prox1-EGFP$^+$ mice injected with Rhod6G (red) shows that SLYM (EGFP$^+$, green) is permeated by myeloid cells similar to dura (collagen fibers, gray). Middle panels show orthogonal sections depicting Rhod6G $^+$ cells in dura and SLYM, respectively. (Right) In vivo quantification of the number of Rhod6G$^+$ cells present in dura and SLYM. Values are expressed as mean ± SEM, two-tailed unpaired *t* test with Welch's correction, P = 0.5748, n = 7 mice. (**B**) Representative image showing the accumulation of CD45$^+$ cells along the pial vessels. (**C**) The percentage of area covered by CD45$^+$ cells was significantly increased both in aged (12- to 13-month-old) mice and in response to inflammation (LPS 4 mg/kg, ip, 24 hours). Values are expressed as mean ± SEM, two-tailed unpaired *t* test with Welch's correction, $P < 0.005$, n = 3 mice. (**D**) LYVE1 macrophages were also found in the SLYM layer, being more prominent in aged and LPS-treated animals than in healthy young Prox1-EGFP mice. (**E**) The mannose receptor CD206 was detected at similar levels in the young, aged, and LPS-treated groups, suggesting that SLYM may act as a niche for border-associated mouse macrophages. Significance shown as $^*P < 0.05$. Ctr, control.

in the control group, $CD45^+$ cells were abundant, located mostly along pial vessels in the surface of the brain (Fig. 5B). This observation, together with the significant increase in $CD45^+$ in inflammation-prone conditions [aging and lipopolysaccharide (LPS)–treated mice, 4 mg/kg of body weight, intraperitoneally (ip), 24 hours] (Fig. 5C), suggests that SLYM can act as a $CD45^+$ recruiting and/or proliferating site in pathological conditions. Of note, the dose of LPS used (4 mg/kg) did not affect the BBB (fig. S8). Additional immune markers showed that $LYVE1^+$ (Fig. 5D), $CD206^+$ (Fig. 5E), and $CD68^+$ (fig. S9) macrophages can be found in SLYM, together with dendritic cells ($CD11c^+$) (fig. S9). Despite the absence of $CD3^+$ and $CD19^+$ lymphocytes (fig. S9), our results indicate that SLYM functions as a niche for immunological surveillance. Thus, in young, healthy mice, SLYM hosts $CD45^+$ cells, but the number and diversity of innate immune cells rapidly expands in LPS-induced inflammation and was also significantly altered in aged mice. We conclude that SLYM fulfills the characteristics of a mesothelium by acting as an immune barrier that prevents exchange of small solutes between the outer and inner subarachnoid space compartments and by covering blood vessels in the subarachnoid space.

Discussion

The critical roles of the meningeal membranes lining the brain have only recently been acknowledged (*5*, *37*). It is now known that CSF is drained by a network of lymphatic vessels in the meninges and that suppression of this drainage accelerates protein aggregation and cognitive decline in animal models of neurodegeneration (*38*–*40*). SLYM is $Prox1^+$/$PDPN^+$/$LYVE1^-$/$CRABP2^+$/$VEGFR3^-$/$CLDN\text{-}11^-$/$E\text{-}Cad^-$ and thereby distinct from the traditional meningeal membranes, including dura, arachnoid, and pia, as well as the meningeal lymphatic vessels and the arachnoid trabecula. SLYM subdivides the subarachnoid space into two compartments, suggesting that CSF transport is more organized than currently acknowledged. For example, SLYM covering the vasculature in the inner subarachnoid space will guide CSF influx along the penetrating arterioles into the brain parenchyma without circulating solutes present in the outer subarachnoid space compartment. Yet the discovery of a fourth meningeal layer, SLYM, has several implications beyond fluid transport. The observation that SLYM is a barrier for CSF solutes that have a molecular weight larger than 3 kDa will require more detailed studies but indicates a need to redefine the concept of CNS barriers to include SLYM. The meningeal membranes are hosts to myeloid cells responsible for immune surveillance of the CNS (*5*, *37*), and SLYM, owing to its close association with the brain surfaces, is likely to play a prominent role in this surveillance. Herein, we showed a large increase in the number and diversity of immune cells residing in SLYM in response to acute inflammation and natural aging. Physical rupture of SLYM could, by altering CSF flow patterns, explain the prolonged suppression of glymphatic flow after traumatic brain injury as well as the heightened posttraumatic risk of developing Alzheimer's disease (*41*, *42*). Rupture of SLYM will also permit the direct passage of immune cells from the skull bone marrow (*33*, *43*) into the inner subarachnoid space, with direct access to the brain surfaces, possibly explaining the prolonged neuroinflammation after traumatic brain injury (*44*). SLYM may also be directly involved in CNS immunity, in addition to being host to many immune cells. Lymphatic-like tissues can transform quickly in the setting of inflammation, which in the brain may be of notable relevance for diseases such as multiple sclerosis (*45*).

REFERENCES AND NOTES

1. J. J. Iliff *et al.*, *Sci. Transl. Med.* **4**, 147ra111 (2012).
2. H. Mestre *et al.*, *Nat. Commun.* **9**, 4878 (2018).
3. N. E. Fultz *et al.*, *Science* **366**, 628–631 (2019).
4. H. Mestre *et al.*, *eLife* **7**, e40070 (2018).
5. A. Louveau *et al.*, *Nature* **523**, 337–341 (2015).
6. A. Aspelund *et al.*, *J. Exp. Med.* **212**, 991–999 (2015).
7. L. H. Weed, *J. Anat.* **72**, 181–215 (1938).
8. A. Key, G. Retzius, *Studien in der Anatomie des Nervensystems und des Bindegewebes* (Samson & Wallin, 1876).
9. W. E. le Gros Clark, *J. Anat.* **55**, 40–48 (1920).
10. K. Ohta *et al.*, *Kurume Med. J.* **49**, 177–183 (2002).
11. M. K. Rasmussen, H. Mestre, M. Nedergaard, *Physiol. Rev.* **102**, 1025–1151 (2022).
12. A. Drieu *et al.*, *Nature* **611**, 585–593 (2022).
13. I. Choi *et al.*, *Blood* **117**, 362–365 (2011).
14. J. T. Wigle *et al.*, *EMBO J.* **21**, 1505–1513 (2002).
15. K. Masamoto *et al.*, *Neuroscience* **212**, 190–200 (2012).
16. A. Nimmerjahn, F. Kirchhoff, J. N. Kerr, F. Helmchen, *Nat. Methods* **1**, 31–37 (2004).
17. K. Kothur, L. Wienholt, F. Brilot, R. C. Dale, *Cytokine* **77**, 227–237 (2016).
18. H. Mestre, Y. Mori, M. Nedergaard, *Trends Neurosci.* **43**, 458–466 (2020).
19. M. Tomooka, C. Kaji, H. Kojima, Y. Sawa, *Acta Histochem. Cytochem.* **46**, 171–177 (2013).
20. S. Banerji *et al.*, *J. Cell Biol.* **144**, 789–801 (1999).
21. M. A. Asson-Batres, O. Ahmad, W. B. Smith, *Cell Tissue Res.* **312**, 9–19 (2003).
22. C. B. Brøchner, C. B. Holst, K. Møllgård, *Front. Neurosci.* **9**, 75 (2015).
23. J. DeSisto *et al.*, *Dev. Cell* **54**, 43–59.e4 (2020).
24. J. Derk, H. E. Jones, C. Como, B. Pawlikowski, J. A. Siegenthaler, *Front. Cell. Neurosci.* **15**, 703944 (2021).
25. M. M. Mortazavi *et al.*, *World Neurosurg.* **111**, 279–290 (2018).
26. S. E. Mutsaers, F. J. Pixley, C. M. Prêle, G. F. Hoyne, *Curr. Opin. Immunol.* **64**, 88–109 (2020).
27. B. A. Hills, J. R. Burke, K. Thomas, *Perit. Dial. Int.* **18**, 157–165 (1998).
28. A. Jayatilaka, *Ceylon J. Med. Sci.* **18**, 25–30 (1969).
29. D. G. Potts, V. Deonarine, *J. Neurosurg.* **38**, 722–728 (1973).
30. K. Suzuki *et al.*, *Nat. Commun.* **7**, 13718 (2016).
31. Y. Su *et al.*, *Nat. Methods* **17**, 852–860 (2020).
32. M. P. Hall *et al.*, *ACS Chem. Biol.* **7**, 1848–1857 (2012).
33. J. Rustenhoven *et al.*, *Cell* **184**, 1000–1016.e27 (2021).
34. P. Mastorakos, D. McGavern, *Sci. Immunol.* **4**, eaav0492 (2019).
35. H. Baatz, M. Steinbauer, A. G. Harris, F. Krombach, *Int. J. Microcirc. Clin. Exp.* **15**, 85–91 (1995).
36. A. Merlini *et al.*, *Nat. Neurosci.* **25**, 887–899 (2022).
37. A. Louveau *et al.*, *J. Clin. Invest.* **127**, 3210–3219 (2017).
38. S. Da Mesquita, Z. Fu, J. Kipnis, *Neuron* **100**, 375–388 (2018).
39. Z. Xu *et al.*, *Mol. Neurodegener.* **10**, 58 (2015).
40. L. Wang *et al.*, *Brain Pathol.* **29**, 176–192 (2019).
41. A. Z. Mohamed, P. Cumming, J. Götz, F. Nasrallah; Department of Defense Alzheimer's Disease Neuroimaging Initiative, *Eur. J. Nucl. Med. Mol. Imaging* **46**, 1139–1151 (2019).
42. J. D. Flatt, P. Gilsanz, C. P. Quesenberry Jr., K. B. Albers, R. A. Whitmer, *Alzheimers Dement.* **14**, 28–34 (2018).
43. S. Brioschi *et al.*, *Science* **373**, eabf9277 (2021).
44. J. J. Iliff *et al.*, *J. Neurosci.* **34**, 16180–16193 (2014).
45. N. B. Pikor, A. Prat, A. Bar-Or, J. L. Gommerman, *Front. Immunol.* **6**, 657 (2016).

ACKNOWLEDGMENTS

We acknowledge P. S. Froh and H. Nguyen (Department of Cellular and Molecular Medicine, Faculty of Health and Medical Sciences, University of Copenhagen, Denmark) for their excellent technical assistance for the histology and immunohistochemistry of the decalcified samples. We also thank D. Xue for expert graphical support, B. Sigurdsson for analysis, and H. Hirase, N. Cankar, and N. C. Petersen for critical reading of the manuscript. **Funding:** Funding was provided by Lundbeck Foundation grant R386-2021-165 (M.N.), Novo Nordisk Foundation grant NNF20OC0066419 (M.N.), the Vera & Carl Johan Michaelsen's Legat Foundation (K.M.), National Institutes of Health grant R01AT011439 (M.N.), National Institutes of Health grant U19NS128613 (M.N.), US Army Research Office grant MURI W911NF1910280 (M.N.), Human Frontier Science Program grant RGP0036 (M.N.), the Dr. Miriam and Sheldon G. Adelson Medical Research Foundation (M.N.), and Simons Foundation grant 811237 (M.N.). The views and conclusions contained in this article are solely those of the authors and should not be interpreted as representing the official policies, either expressed or implied, of the National Institutes of Health, the Army Research Office, or the US Government. The US Government is authorized to reproduce and distribute reprints for Government purposes notwithstanding any copyright notation herein. The funding agencies have taken no part on the design of the study, data collection, analysis, interpretation, or in writing of the manuscript. **Author contributions:** K.M. and M.N. designed the study. F.R.M.B., P.K., L.M.M., C.D., V.P., M.K.R., R.S.G., N.L.H., T.E., and Y.M. performed the experiments, collected the data, and performed the analysis. K.M. and M.N. wrote the manuscript. All authors read and approved the final version of the manuscript. **Competing interests:** The authors declare that they have no competing interests. **Data and materials availability:** All data are available in the main text or the supplementary materials.

SUPPLEMENTARY MATERIALS

science.org/doi/10.1126/science.adc8810
Materials and Methods
Figs. S1 to S9
Table S1
References (*46*–*54*)
MDAR Reproducibility Checklist
Movie S1

View/request a protocol for this paper from *Bio-protocol*.

Submitted 6 May 2022; resubmitted 13 September 2022
Accepted 7 December 2022
10.1126/science.adc8810